Dalton Transactions

ROYAL SOCIETY OF CHEMISTRY

PAPER

View Article Online
View Journal | View Issue

Cite this: *Dalton Trans.*, 2023, **52**, 17315

Spectrally tunable near-infrared photoluminescence in $MP_3O_9:Cr^{3+}$ (M = Al, Ga, In) phosphate phosphors

Lipeng Jiang,[a] Xue Jiang,*[a,d] Liangliang Zhang,[b] Guocai Lv[c] and Yanjing Su*[a]

Received 4th September 2023,
Accepted 26th October 2023

DOI: 10.1039/d3dt02882h

rsc.li/dalton

Modulation of the octahedral crystal field environment of Cr^{3+} is an effective approach to achieve tunable emission. Here, we prepared a series of broadband $MP_3O_9:Cr^{3+}$ (M = Al, Ga, In) near-infrared (NIR) phosphors, and cubic $AlP_3O_9:Cr^{3+}$ (APO-c:Cr^{3+}) and monoclinic $AlP_3O_9:Cr^{3+}$ (APO-m:Cr^{3+}) phosphors were prepared by controlling the synthesis temperature. The emission wavelength was tuned from 787 nm for APO-c:Cr^{3+} to 894 nm for monoclinic $InP_3O_9:Cr^{3+}$ (IPO:Cr^{3+}) by regulating the M ion and reducing the crystal field intensity. Excitingly, the $MP_3O_9:Cr^{3+}$ (M = Al, Ga, In) family shows excellent thermal stability; the emission intensity of APO-c:Cr^{3+}, APO-m:Cr^{3+} and monoclinic $GaP_3O_9:Cr^{3+}$ (GPO:Cr^{3+}) can still maintain 95.6%, 86% and 86% of that at room temperature when heating to 423 K, respectively. An NIR LED device was prepared by incorporating GPO:Cr^{3+} and a blue light LED, demonstrating the potential application in night vision and non-destructive testing.

1. Introduction

Near-infrared (NIR) spectroscopy is extensively used in night vision, health monitoring, non-destructive testing, and biological imaging due to its convenient and fast response characteristics.[1–5] The route of combining blue LEDs with NIR phosphors has been proven to be an effective and feasible approach, benefiting from the rich experience acquired during the development and application of white LEDs.[6–8] The phosphor performance almost ultimately determines the device performance; therefore, the development of broadband NIR phosphors that are thermally stable and can be efficiently excited by InGaN LED chips is crucial.[9–11]

The transition metal ion Cr^{3+} is considered as an ideal broadband NIR activator.[12–15] Firstly, Cr^{3+} has good absorption in the blue region and can be perfectly matched with blue chips. Additionally, the emission of Cr^{3+} depends on the octahedral crystal field, and a wide range of emission spectra can be tuned by modulating the octahedral crystal field strength.[16–19] Taking advantage of this property, researchers have developed many Cr^{3+}-activated NIR-emitting materials, and these studies have focused on aluminates, borates, niobates/tantalates, *etc.*[20–23] For instance, in our previous study, we replaced the Al^{3+}–Ga^{3+} pair with Mg^{2+}–Ge^{4+} in $Gd_3Al_2Ga_3O_{12}:Cr^{3+}$, and the emission wavelength shifted from 729 nm to 805 nm.[24] Zhang *et al.* reported $ABO_4:Cr^{3+}$ (A = Ga, Sc, In; B = Ta, Nb) NIR phosphors, which achieved wide spectral tuning from NIR-I to NIR-II with the peak position from 825 nm to 1025 nm by cation replacement.[25] Zhong *et al.* achieved an emission peak redshift from 726 nm to 830 nm by replacing the Ga^{3+}–Ga^{3+} unit with Mg^{2+}–Ge^{4+} in the Ga_2O_3 structure.[26]

Recently, Cr^{3+}-activated phosphates have attracted much attention due to the simple preparation method and the low price of raw materials.[27–30] The weak crystal field generated by their relatively relaxed crystal structure offers the possibility for achieving broadband NIR emission. Researchers have reported a variety of Cr^{3+}-doped phosphate NIR phosphors. For example, several researchers reported AMP_2O_7 (A = Li, Na, K; M = Al, Ga, Sc, In) phosphors, which can be tuned in the 780–900 nm range by varying the A and M ions.[31–35] Zhao *et al.* reported $Sr_9M(PO_4)_7:Cr^{3+}$ (M = Ga, Sc, In) phosphors, and investigated the effect of structural constraints on the luminescence performance.[36] Miao *et al.* reported tunable broadband NIR photoluminescence by co-doping Ga^{3+} in $Na_3Sc_2(PO_4)_3:Cr^{3+}$ phosphors.[37] Unfortunately, almost all developed phosphate phosphors exhibit poor thermal stability.

In this paper, we report a series of $MP_3O_9:Cr^{3+}$ (M = Al, Ga, In) NIR phosphate phosphors. The effect of the synthesis temperature on the $AlP_3O_9:Cr^{3+}$ phase transition was investigated. A wide range of spectral tuning (787–894 nm) was achieved by

[a]*Beijing Advanced Innovation Center for Materials Genome Engineering, Corrosion and Protection Center, University of Science and Technology Beijing, Beijing, 100083, China. E-mail: jiangxue@ustb.edu.cn, yjsu@ustb.edu.cn*
[b]*State Key Laboratory of Luminescence and Applications, Changchun Institute of Optics, Fine Mechanics and Physics, Chinese Academy of Sciences, 3888 Eastern South Lake Road, Changchun 130033, China*
[c]*Basic Experimental Center of Natural Science, University of Science and Technology Beijing, Beijing, 100083, China*
[d]*Collaborative Innovation Center of Steel Technology, University of Science and Technology Beijing, 100083 Beijing, China*

varying the M ion. In addition, the $MP_3O_9:Cr^{3+}$ (M = Al, Ga) family shows excellent thermal stability; the emission intensity of cubic $AlP_3O_9:Cr^{3+}$ (APO-c:Cr^{3+}), monoclinic $AlP_3O_9:Cr^{3+}$ (APO-m:Cr^{3+}) and monoclinic $GaP_3O_9:Cr^{3+}$ (GPO:Cr^{3+}) can still maintain 95.6%, 86% and 86% of that at room temperature when heated to 423 K, respectively. NIR LED devices prepared using GPO:Cr^{3+} for night vision and non-destructive testing confirmed that $MP_3O_9:Cr^{3+}$ (M = Al, Ga, In) are promising NIR phosphors.

2. Materials preparation and characterization

The $MP_3O_9:0.04Cr^{3+}$ (M = Al, Ga, In) phosphors were obtained by a solid state reaction method. Al_2O_3 (99.99%), Ga_2O_3 (99.99%), In_2O_3 (99.99%), $NH_4H_2PO_4$ (99%), and Cr_2O_3 (99.99%) were taken as raw materials. All the raw materials were weighed according to the chemical formula and then mixed and ground for 20 min. The raw materials were held in a muffle furnace at 500 °C for 2 h, and then heated up again to 800–1000 °C for 5 h. After cooling down, the $MP_3O_9:0.04Cr^{3+}$ (M = Al, Ga, In) phosphors were obtained.

The NIR LED devices were fabricated by coating blue LED chips (450–460 nm) with a mixture of the prepared phosphors and silicone (A : B = 1 : 4). The devices were further cured at 100 °C for 1 h and 150 °C for 2 h in an oven.

The XRD curves were obtained using an X'PERT PRO MPD X-ray diffractometer. The emission spectra, excitation spectra, temperature dependent emission spectra and luminescence decay times were acquired *via* an FLS-1000 fluorescence spectrophotometer. The absolute PL QY measurement (Hamamatsu C9920-02) was applied to obtain the IQE, a 450 nm laser was used as excitation sources for $MP_3O_9:0.04Cr^{3+}$ (M = Al, Ga) and a xenon lamp was used as the excitation source for $InP_3O_9:Cr^{3+}$. The fabricated LED's output power was evaluated using an OHSP-350M (Hopoo Optoelectronics Co., Ltd, 350–1050 nm). Meanwhile, photographs were acquired using an industrial USB night vision camera (Shenzhen Zhongweiaoke Technology Co. Ltd, 1080 P, 700–1100 nm, China) to demonstrate the application of NIR pc-LEDs.

3. Results and discussion

3.1. Crystal structure of $MP_3O_9:Cr^3$

Fig. 1a displays the XRD patterns of $AlP_3O_9:Cr^{3+}$ obtained at different sintering temperatures. By comparing with the standard card, it is found that the sample obtained at 900 °C contains both cubic AlP_3O_9 (AIP-c) and monoclinic AlP_3O_9 (AIP-m). The sample sintered at 1000 °C shows cubic phase, which corresponds to the standard card ICSD#26759, and the sample sintered at 800 °C shows monoclinic phase, which corresponds to the standard card ICSD#170. This indicates that the material system undergoes a phase transition from AIP-m to AIP-c with increasing temperature. A small amount of $AlPO_4$ (ICSD#16651) phase appeared in the sample due to the decomposition of phosphate at high temperature. According to the domain knowledge, Cr^{3+} preferentially occupies the [AlO_6] octahedral site, while $AlPO_4$ assumes the [AlO_4] tetrahedral structure; hence the presence of $AlPO_4$ exerts no influence on the photoluminescence property.

The XRD patterns of monoclinic $MP_3O_9:Cr^{3+}$ (M = Al, Ga, In) phosphors are given in Fig. 1b. The diffraction peaks shift to a lower angle when the M ion changes from Al to In, which is attributed to the lattice expansion caused by the increase of the M ion radius. As shown in Fig. 1d, the average M–O bond length in the [MO_6] octahedron increases gradually as the M

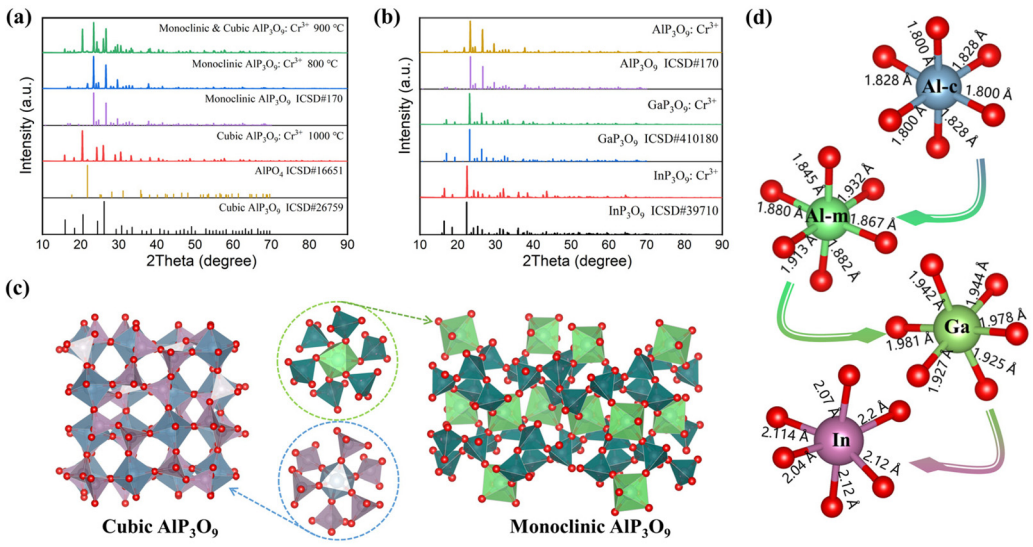

Fig. 1 (a) XRD patterns of cubic AlP_3O_9 and monoclinic AlP_3O_9. (b) XRD patterns of monoclinic $MP_3O_9:0.04Cr^{3+}$ (M = Al, Ga, In). (c) Crystal structure and coordination environment of AlO_6 octahedra of cubic AlP_3O_9 and monoclinic AlP_3O_9. (d) The M–O bond length of MP_3O_9 (M = Al, Ga, In). Al-cO_6 and Al-mO_6 are octahedra in cubic and monoclinic AlP_3O_9, respectively.

ion changes from Al to In. The diffraction angle decreases when the crystal plane spacing d increases according to the Bragg equation $2d\sin\theta = n\lambda$. The crystal structure and coordination environment of [AlO_6] octahedra of cubic AlP_3O_9 and monoclinic AlP_3O_9 are given in Fig. 1c. In the MP_3O_9 crystal structure, the [MO_6] octahedron is surrounded by six [PO_4] tetrahedra, forming a larger [MP_6] octahedron by sharing O ions with dot connections. The average M–O bond length of the [MO_6] octahedron increases gradually (Fig. 1d), which enables the change of the local crystal field environment and thus the tuning of the emission spectrum.

3.2. Octahedron-dependent tunable photoluminescence

Fig. 2a shows the emission and excitation spectra of MP_3O_9:Cr^{3+} (M = Al, Ga, In). The excitation spectra of MP_3O_9:Cr^{3+} phosphors exhibit two excitation bands at 400–500 nm and 600–800 nm, corresponding to the $^4A_{2g} \rightarrow {}^4T_{1g}$ and $^4A_{2g} \rightarrow {}^4T_{2g}$ transitions of Cr^{3+}, respectively. The emission spectra that cover 600–1300 nm originate from the $^4T_{2g} \rightarrow {}^4A_{2g}$ transition of Cr^{3+}. With the sequential changes of M ions from Al to Ga and In, the emission spectrum is gradually red-shifted, and the emission peak position is red-shifted from 787 nm to 894 nm. The redshift of the emission spectrum is associated with a decrease in the intensity of the crystal field. The crystal field intensity can be calculated by eqn (1):[38,39]

$$D_q = \frac{1}{6} Ze^2 \frac{r^4}{R^5} \quad (1)$$

where D_q, Z, e, r and R are the crystal field strength, anion charges, electron charges, the radius of the d-wave function and the Cr–O bond length, respectively. According to the analysis of Fig. 1d, the Cr–O bond length increases gradually from APO-c to IPO, leading to a decrease in D_q.

In general, it exhibits broadband emission when Cr^{3+} is in a weak crystal field environment. The strongness of the crystal field environment can be evaluated by D_q/B, where D_q is the crystal field strength and B is the Racah parameter. It is generally accepted that the criterion for a weak crystal field environment is $D_q/B < 2.3$; eqn (2) can be used to calculate D_q/B.[6,40]

$$\begin{aligned} 10 \cdot D_q &= E_a({}^4T_{2g}) \\ \frac{D_q}{B} &= \frac{15 \cdot (x-8)}{x^2 - 10 \cdot x} \\ D_q \cdot x &= E_a({}^4T_{1g}) - E_a({}^4T_{2g}) \end{aligned} \quad (2)$$

where $E_a(^4T_{1g})$ and $E_a(^4T_{2g})$ are the energy positions of $^4T_{1g}$ and $^4T_{2g}$, respectively. In this study, $E_a(^4T_{2g})$ was calculated as the median of the peak energies of the $^4A_{2g} \rightarrow {}^4T_{2g}$ excitation band and $^4T_{2g} \rightarrow {}^4A_{2g}$ emission band, taking into account the correlation between the Stokes shift and bandwidth. The calculated D_q/B of APO-c:Cr^{3+}, APO-m:Cr^{3+}, GPO:Cr^{3+}, and IPO:Cr^{3+} are 1.66, 1.57, 1.51, and 1.44, respectively. Thus, the emission spectra of MP_3O_9:Cr^{3+} (M = Al, Ga, In) all show broadband emission. The detailed photoluminescence parameters can be found in Table 1.

The relationship between the emission intensity of MP_3O_9:Cr^{3+} (M = Al, Ga, In) phosphors and the M ion is depicted in Fig. 2b. The photoluminescence intensity decreases gradually when the M ion changes from Al to In. Meanwhile, the full widths at half maximum (FWHM) of their emission bands increase gradually. The FWHMs of APO-c:Cr^{3+}, APO-m:Cr^{3+}, GPO:Cr^{3+}, and IPO:Cr^{3+} are 120 nm, 139 nm, 141 nm, and 166 nm, respectively. The broadened FWHM indicates a strong electron–phonon coupling effect, and in this case, non-radiative decay depends on the Stokes shift ΔR. As M changes from Al to In, the ΔR gradually increases (Table 1), leading to an

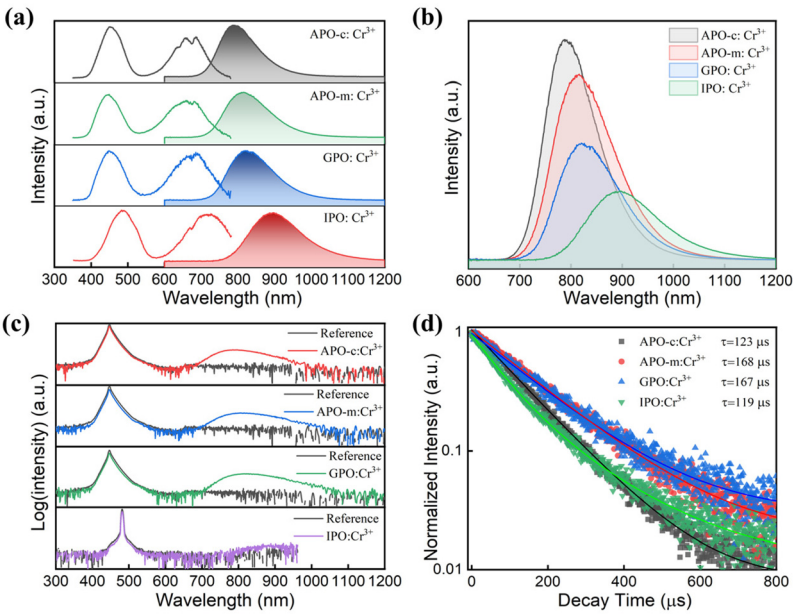

Fig. 2 (a) Normalized emission and excitation spectra, (b) comparison of the emission intensity, (c) IQE and (d) decay times of MP_3O_9:Cr^{3+} (M = Al, Ga, In).

Table 1 PL properties of Cr^{3+}-doped $MP_3O_9:Cr^{3+}$ (M = Al, Ga, In) NIR phosphors

Phosphors	λ_{ex} (nm)	λ_{em} (nm)	D_q (cm^{-1})	B (cm^{-1})	ΔR (cm^{-1})	D_q/B
APO-c:Cr^{3+}	450/670	787	1384	834	2263	1.66
APO-m:Cr^{3+}	450/672	813	1359	866	2580	1.57
GPO:Cr^{3+}	450/676	819	1350	892	2582	1.51
IPO:Cr^{3+}	480/725	894	1249	867	2607	1.44

increase in the non-radiative transition probability, resulting in a decrease in the emission intensity.[31] Accordingly, the IQE of APO-c:Cr^{3+}, APO-m:Cr^{3+}, GPO:Cr^{3+}, and IPO:Cr^{3+} are 43.5%, 33.6%, 30.2% and 19.8%, respectively (Fig. 2c). Fig. 2d shows the decay curves of $MP_3O_9:Cr^{3+}$ (M = Al, Ga, In) phosphors. All the decay curves can be fitted well by single exponential function, which illustrates that the NIR emission at room temperature stems from one luminescence center. The lifetime of APO-c:Cr^{3+} is calculated to be 123 μs, which is at the same level as previously reported.[41] The lifetimes of APO-m:Cr^{3+}, GPO:Cr^{3+}, and IPO:Cr^{3+} are 168 μs, 167 μs, and 119 μs, respectively. The lifetime of APO-c:Cr^{3+} is shorter than that of monoclinic $MP_3O_9:Cr^{3+}$ (M = Al, Ga, In), indicating that APO-c:Cr^{3+} suffers from stronger nonradiative relaxation at room temperature.[42]

3.3. Temperature-dependent luminescence of $MP_3O_9:Cr^3$

The thermal stability of phosphors is crucial for their applications, especially phosphate phosphors, which generally suffer from the challenge of poor thermal stability.[43,44] The emission spectra of $MP_3O_9:Cr^{3+}$ (M = Al, Ga, In) phosphors at different temperatures are displayed in Fig. 3a–d. The emission intensity decreases with increasing temperature, which is due to thermal quenching. The integrated intensity of APO-c:Cr^{3+} remains at 95.3% of that at room temperature when heating to 423 K, which is the highest value reported so far for Cr^{3+}-activated phosphate materials such as $KAlP_2O_7:Cr^{3+}$ (77% @423 K),[33] $KGaP_2O_7:Cr^{3+}$ (56%@423 K),[34] and $Na_3Sc_2(PO_4)_3:Cr^{3+}$ (84%@423 K).[37] The integrated intensity of monoclinic $MP_3O_9:Cr^{3+}$ (M = Al, Ga, In) phosphors at 423 K maintains 86%, 86%, and 38% of that at room temperature, respectively, which are also superior to those of most phosphate NIR phosphors (Fig. 3e).

The temperature dependent emission peak positions of both APO-c:Cr^{3+} and APO-m:Cr^{3+} phosphors exhibit a small red shift, which is attributed to the lattice expansion with increasing temperature. In addition, the FWHM of the emission spectrum changes significantly with increasing temperature, and the broadening of the FWHM at high temperature is associated with the electron–phonon coupling effect. The Huang–Rhys factor (S) can be used to reflect the variation of electron–phonon coupling, which can be calculated by the following equation:[45]

$$\mathrm{FWHM} = 2.36\sqrt{S}\hbar\omega\sqrt{\coth\left(\frac{\hbar\omega}{2kT}\right)} \quad (3)$$

where $\hbar\omega$ and k are the effective phonon energy and Boltzmann constant, respectively. Eqn (3) reflects the variation of the FWHM with temperature, and it can be simplified as eqn (4).

$$\mathrm{FWHM}^2 = 5.57 \times S \times (\hbar\omega)^2\left[1 + \frac{1}{\hbar\omega/2KT}\right] \quad (4)$$

Then, if we let $a = 5.57 \times S \times (\hbar\omega)^2$ and $b = 5.57 \times S \times \hbar\omega$, eqn (4) can be further simplified as eqn (5).

$$\mathrm{FWHM}^2 = a + \frac{b}{1/(2KT)} \quad (5)$$

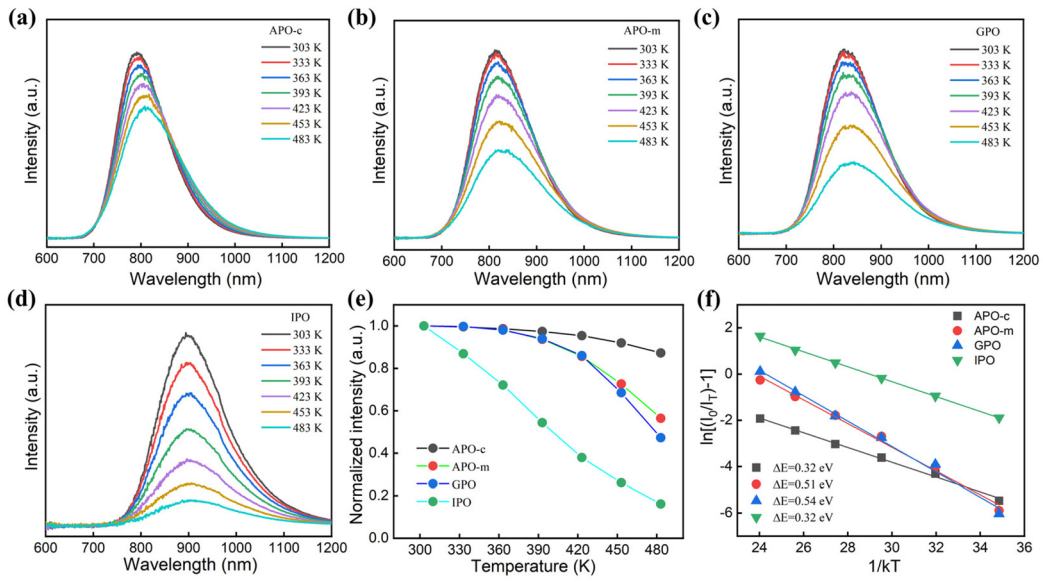

Fig. 3 The emission spectra of (a) APO-c:Cr^{3+}, (b) APO-m:Cr^{3+}, (c) GPO:Cr^{3+}, and (d) IPO:Cr^{3+} at 303–483 K. (e) Normalized emission intensity at different temperatures and (f) the calculated activation energy of $MP_3O_9:Cr^{3+}$ (M = Al, Ga, In).

The Huang–Rhys factors of monoclinic $MP_3O_9:Cr^{3+}$ (M = Al, Ga, In) phosphors are calculated to be 4.5, 4.67, and 8.25, respectively, and 8.63 for cubic $AlP_3O_9:Cr^{3+}$(Fig. 4). Generally, the stronger the electron–phonon coupling effect, the larger the lattice relaxation, and the thermal quenching activation energy (ΔE) is smaller. The activation energy (ΔE) can be obtained by the Arrhenius equation (eqn 6).[46–48]

$$I_T = \frac{I_0}{1 + C\exp\left(-\frac{\Delta E}{kT}\right)} \quad (6)$$

where I_T denotes the emission intensity of the sample at temperature T, and I_0, k and C are the initial emission intensity, Boltzmann constant and constant, respectively. The activation energies of monoclinic $MP_3O_9:Cr^{3+}$ (M = Al, Ga, In) phosphors are 0.51 eV, 0.54 eV and 0.32 eV, respectively, and 0.32 eV for APO-c:Cr^{3+} (Fig. 3f). These values are higher than those of previously reported phosphate phosphors such as $KAlP_2O_7:Cr^{3+}$ (0.292 eV),[33] $AlP_3O_9:Cr^{3+}$ (0.29 eV),[41] $KGaP_2O_7:Cr^{3+}$ (0.3 eV),[34] and $LiGe_2(PO_4)_3:Cr^{3+}$.[27] The decrease in activation energy when M changes from Al to In is attributed to the large Stokes shift that reduces the energy difference between the lowest point of the excited state and the intersection of ground and excited states. The decrease in activation energy will reduce the energy barrier for non-radiative transitions, leading to a decrease in thermal stability. The changes of the activation energy and Huang–Rhys factor in monoclinic $MP_3O_9:Cr^{3+}$ (M = Al, Ga, In) phosphors are observed to coincide with the trend of thermal stability. Hence, the enhanced electron–phonon coupling effect and the reduced energy barrier contribute together to the reduced thermal stability of monoclinic $MP_3O_9:Cr^{3+}$ (M = Al, Ga, In) phosphors when M changes from Al to In.

APO-c:Cr^{3+} exhibits excellent thermal stability; however, it suffers from a larger electron–phonon coupling effect and a lower activation energy compared with APO-m:Cr^{3+}. This paradox may suggest that the electron–phonon coupling associated with the nonradiative transition plays a non-dominant role in the thermal quenching of APO-c:Cr^{3+}. In a recent work, Huang *et al.* attributed the excellent thermal stability of APO-c:Cr^{3+} phosphors to negligible thermal expansion, which is well supported by their experimental data.[41] In fact, the thermal stability of the phosphor exhibited is the result of the combined effect of the band gap, electron–phonon coupling, structural rigidity, *etc*. As we analyzed in Fig. 1c, the $[MO_6]$ octahedron is surrounded by six $[PO_4]$ tetrahedra in the MP_3O_9 crystal, forming a larger $[MP_6]$ octahedron. This unique structure may give $[MO_6]$ great rigidity, which may explain its excellent thermal stability. As shown in Fig. 1d, APO-c:Cr^{3+} possesses a more compact octahedral environment compared to monoclinic $MP_3O_9:Cr^{3+}$ (M = Al, Ga, In), suggesting a rigid structure. The minimum Stokes shift also confirms this, as the Stokes shift is strongly affected by the rigidity of the crystal structure. Further research is needed on the thermal quenching mechanism of the MPO-c:Cr^{3+} family. To summarize, $MP_3O_9:Cr^{3+}$ (M = Al, Ga, In) phosphors all show good thermal stability and can be considered as candidate materials for NIR LEDs.

3.4. Photoluminescence of $GaP_3O_9:xCr^{3+}$

Comprehensively considering the luminescence intensity, thermal stability and wavelength, the $GaP_3O_9:Cr^{3+}$ phosphor was selected for a detailed investigation. To optimize the Cr^{3+}-doping concentration, GPO:xCr^{3+} (x = 0.01–0.1) were prepared. The XRD patterns of GPO:xCr^{3+} are presented in Fig. 5a. All the XRD patterns agree with the standard card, proving the successful realization of the pure phase. With increasing doping concentration, the emission intensity increases first and then decreases, and x = 0.06 was identified as the optimum doping concentration (Fig. 5b). The decrease in intensity at a high doping concentration is attributed to concentration quenching. In addition, the lifetime gradually decreases from 168.2 μs to 163 μs with increasing Cr^{3+} concentration, suggesting that the possibility of nonradiative transitions increases with increasing Cr^{3+} concentration (Fig. 5c).

The temperature dependent emission spectra of the optimal doping concentration sample are given in Fig. 5d.

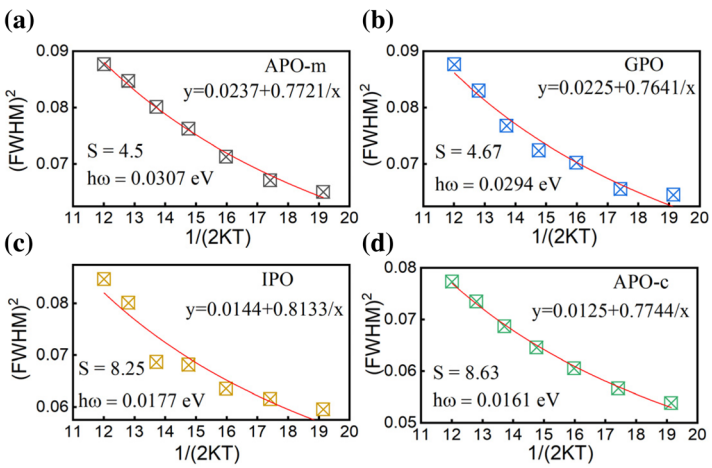

Fig. 4 Fitting $(FWHM)^2$ and $1/(2KT)$ to obtain the Huang–Rhys factor. (a) APO-m:Cr^{3+}, (b) GPO:Cr^{3+}, (c) IPO:Cr^{3+}, and (d) APO-c:Cr^{3+}.

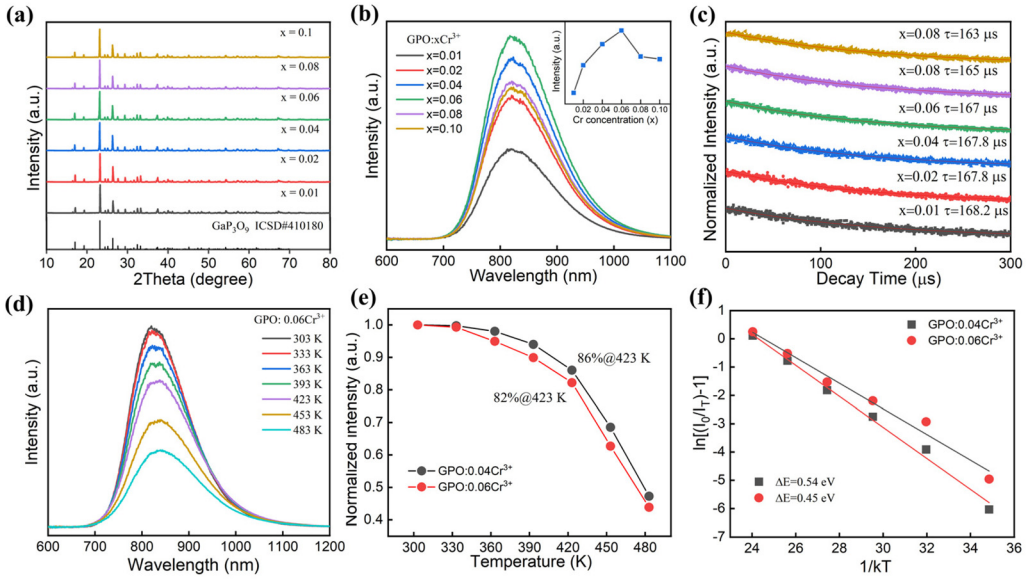

Fig. 5 (a) XRD patterns, (b) emission spectra and (c) decay times of GPO:xCr^{3+}. (d) Temperature-dependent emission spectra of GPO:0.06Cr^{3+}. (e) Normalized emission intensity of GPO:xCr^{3+} (x = 0.04, 0.06) at different temperatures. (f) Activation energy of GPO:xCr^{3+} (x = 0.04, 0.06).

With increasing temperature, the emission peak position is redshifted from 820 to 843 nm and the FWHM is broadened from 139 to 165 nm due to electron–phonon coupling. In addition, Fig. 5e shows the thermal stability of GPO:xCr^{3+} *versus* the doping concentration. The results show that GPO:0.04Cr^{3+} possesses better thermal stability as the probability of energy transfer to the quenching center is low at a low concentration. The activation energies show the same pattern, with the activation energies calculated to be 0.54 and 0.45 eV for GPO:0.04Cr^{3+} and GPO:0.06Cr^{3+} (Fig. 5f). The large activation energies provide energy barriers against non-radiative transitions and ensure excellent thermal stability.

3.5. NIR pc-LED devices and application

To demonstrate the application of our prepared NIR phosphors in the NIR region, GPO:Cr^{3+} was chosen to be combined with 450 nm blue LEDs to prepare NIR LED devices. The emission spectra of the NIR LED device are shown in Fig. 6a. The inset shows the fabricated LED device. The emission spectra contain a narrow band emission of 450 nm blue light and a broadband emission of GPO:Cr^{3+} centered at 820 nm. The emission intensity increases with the increase of the input power, while the photoelectric conversion efficiency increases first and then decreases gradually. The device produces an output power of 26.2 mW when the input power is 288 mW, and the photoelectric conversion efficiency is 9.1% (Fig. 6b).

In addition, we also show the application of the prepared pc-LED in night vision and non-destructive testing, as shown in Fig. 6c. In natural light, a visible camera can take a colored photo of the chemical bottle, but it is not possible to observe the remaining amount of chemicals, and there is no image when it is dark. In contrast, the NIR camera captures a black

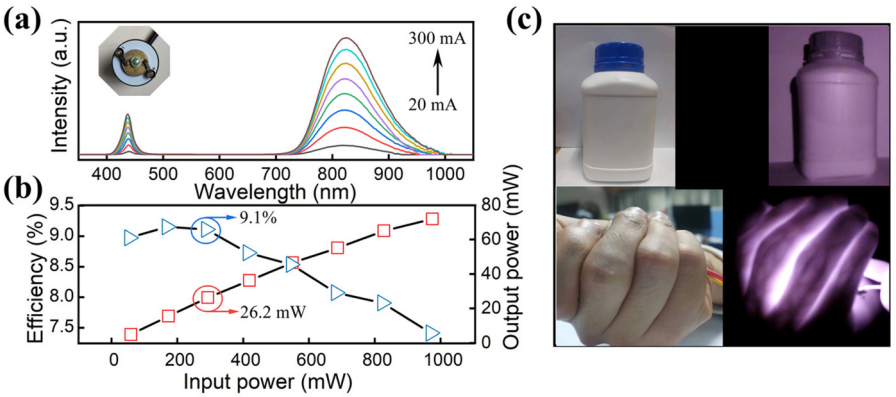

Fig. 6 (a) Electroluminescence spectra of the NIR-pc-LED made using GPO:Cr^{3+} at different input currents. The inset shows the fabricated LED device. (b) The output power and photoelectric conversion efficiency as a function of input power. (c) Application demonstration of the NIR light source.

and white image when illuminated with NIR LEDs. Additionally, benefiting from the excellent penetration, the NIR light source can be used to check the remaining amount of chemicals. NIR light can also easily penetrate the fingers and we can capture the blood vessels with an NIR camera due to the difference in NIR light absorption by human tissues. All these results show that the NIR light source has great potential in night vision and non-destructive testing.

4 Conclusion

In conclusion, a series of broadband $MP_3O_9:Cr^{3+}$ (M = Al, Ga, In) NIR phosphors were successfully synthesized. The phase transition of AlP_3O_9 can be controlled by controlling the sintering temperature, with APO-m formed at 800 °C and APO-c formed at 1000 °C. With the variation of M ions from Al to In, the crystal field intensity decreases gradually and the emission wavelength redshifts from 787 nm to 894 nm. APO-m:Cr^{3+} and GPO:Cr^{3+} exhibit good thermal stability (86%@423 K) owing to their high activation energy and unique rigid structure. APO-c:Cr^{3+} shows excellent thermal stability (95.3%@423 K), and its thermal quenching mechanism still needs further investigation. The NIR device prepared using GPO:Cr^{3+} produces an output power of 26.2 mW when the input power is 288 mW, and the photoelectric conversion efficiency is 9.1%, demonstrating the potential application in night vision and non-destructive testing. Our work provides more promising possibilities to further develop phosphate phosphors with excellent thermal stability.

Conflicts of interest

There are no conflicts to declare.

Acknowledgements

This work was financially supported by the National Key Research and Development Program of China (2021YFB3501500), Guangdong Province Key Area R&D Program (2019B010940001), National Natural Science Foundation of China (52201061, U22A20106), and Fundamental Research Funds for the Central Universities (FRF-TP-22-008A1).

References

1 F. Zhao, Z. Song and Q. Liu, Advances in Chromium-Activated Phosphors for Near-Infrared Light Sources, *Laser Photonics Rev.*, 2022, 2200380.
2 L. Jiang, X. Jiang, J. Xie, H. Sun, L. Zhang, X. Liu, Z. Bai, G. Lv and Y. Su, Ultra-broadband near-infrared $Gd_3MgScGa_2SiO_{12}$: Cr, Yb phosphors: Photoluminescence properties and LED applications, *J. Alloys Compd.*, 2022, **920**, 165912.
3 L. Zhang, S. Zhang, Z. Hao, X. Zhang, G.-H. Pan, Y. Luo, H. Wu and J. Zhang, A high efficiency broad-band near-infrared $Ca_2LuZr_2Al_3O_{12}:Cr^{3+}$ garnet phosphor for blue LED chips, *J. Mater. Chem. C*, 2018, **6**, 4967–4976.
4 L. Zhang, D. Wang, F. Liu, H. Wu, G. Pan, H. Wu, Z. Hao, H. Zhang and J. Zhang, Minimizing Bond Angle Distortion to Improve Thermal Stability of Cr^{3+} Doped Near-Infrared Phosphor, *Laser Photonics Rev.*, 2023, **17**, 2300092.
5 L. Zhang, J. Zhang, Z. Hao, H. Wu, G. Pan, H. Wu and X. Zhang, Recent Progress on Cr^{3+} Doped Broad Band NIR Phosphors, *Chin. J. Lumin.*, 2019, **40**, 1449.
6 H. Xiao, J. Zhang, L. Zhang, H. Wu, H. Wu, G. Pan, F. Liu and J. Zhang, Cr^{3+} Activated Garnet Phosphor with Efficient Blue to Far-Red Conversion for pc-LED, *Adv. Opt. Mater.*, 2021, **9**, 2101134.
7 L. Zhang, D. Wang, Z. Hao, X. Zhang, G.-H. Pan, H. Wu and J. Zhang, Cr^{3+}-Doped Broadband NIR Garnet Phosphor with Enhanced Luminescence and its Application in NIR Spectroscopy, *Adv. Opt. Mater.*, 2019, **7**, 1900185.
8 Y. Jin, Z. Zhou, R. Ran, S. Tan, Y. Liu, J. Zheng, G. Xiang, L. Ma and X.-J. Wang, Broadband NIR Phosphor $Ca_2LuScAl_2Si_2O_{12}:Cr^{3+}$ for NIR LED Applications, *Adv. Opt. Mater.*, 2022, **10**, 2202049.
9 V. Rajendran, M.-H. Fang, G. N. D. Guzman, T. Lesniewski, S. Mahlik, M. Grinberg, G. Leniec, S. M. Kaczmarek, Y.-S. Lin, K.-M. Lu, C.-M. Lin, H. Chang, S.-F. Hu and R.-S. Liu, Super Broadband Near-Infrared Phosphors with High Radiant Flux as Future Light Sources for Spectroscopy Applications, *ACS Energy Lett.*, 2018, **3**, 2679–2684.
10 X. Wu, S. Zhao, L. Zhang, L. Dong, Y. Xu, S. Yin and H. You, Highly thermally stable Cr^{3+} and Yb^{3+} codoped Gd^2GaSbO_7 phosphors for broadband near-infrared applications, *Dalton Trans.*, 2021, **50**, 13459–13467.
11 K. Cheng, Y. Xu, X. Liu, J. Long, W. Huang and C. Deng, A novel far-red phosphors $Li_2ZnTi_3O_8:Cr^{3+}$ for indoor plant cultivation:Synthesis and luminescence properties, *Ceram. Int.*, 2023, **49**(4), 6343–6350.
12 Y. Zhang, Y. Liang, S. Miao, D. Chen, S. Yan and J. Liu, Broadband near-infrared $BaMSi_3O_9:Cr^{3+}$ (M = Zr, Sn, Hf) phosphors for light-emitting diode applications, *Inorg. Chem. Front.*, 2021, **8**, 5186–5194.
13 Y. Wang, Z. Wang, G. Wei, Y. Yang, S. He, J. Li, Y. Shi, R. Li, J. Zhang and P. Li, Highly Efficient and Stable Near-Infrared Broadband Garnet Phosphor for Multifunctional Phosphor-Converted Light-Emitting Diodes, *Adv. Opt. Mater.*, 2022, 2200415.
14 L. Fang, L. Zhang, H. Wu, H. Wu, G. Pan, Z. Hao, F. Liu and J. Zhang, Efficient Broadband Near-Infrared $CaMgGe_2O_6:Cr^{3+}$ Phosphor for pc-LED, *Inorg. Chem.*, 2022, **61**, 8815–8822.
15 L. Jiang, X. Jiang, L. Zhang, Q. Liu, X. Mi, Z. Yu, G. Lv and Y. Su, Broadband Near-Infrared Luminescence in Garnet $Y_3Ga_3MgSiO_{12}$: Cr^{3+} Phosphors, *Inorg. Chem.*, 2023, **62**, 4220–4226.

16 E. T. Basore, W. Xiao, X. Liu, J. Wu and J. Qiu, Broadband Near-Infrared Garnet Phosphors with Near-Unity Internal Quantum Efficiency, *Adv. Opt. Mater.*, 2020, **8**, 2000296.

17 M. Mao, T. Zhou, H. Zeng, L. Wang, F. Huang, X. Tang and R.-J. Xie, Broadband near-infrared (NIR) emission realized by the crystal-field engineering of $Y_{3-x}Ca_xAl_{5-x}Si_xO_{12}:Cr^{3+}$ (x = 0–2.0) garnet phosphors, *J. Mater. Chem. C*, 2020, **8**, 1981–1988.

18 H. Zeng, T. Zhou, L. Wang and R.-J. Xie, Two-Site Occupation for Exploring Ultra-Broadband Near-Infrared Phosphor—Double-Perovskite $La_2MgZrO_6:Cr^{3+}$, *Chem. Mater.*, 2019, **31**, 5245–5253.

19 M. Chen, H. Fan, Z. Lu, J. Song, X. Zhang, Q. Pang, P. Chen and L. Zhou, Energy transfer realizes efficient NIR emitting $Ca_2ScTaO_6:Cr^{3+}$, Yb^{3+} perovskite-structured phosphors, *Ceram. Int.*, 2023, **49**(10), 15717–15725.

20 G. Zheng, W. Xiao, H. Wu, J. Wu, X. Liu and J. Qiu, Near-Unity and Zero-Thermal-Quenching Far-Red-Emitting Composite Ceramics via Pressureless Glass Crystallization, *Laser Photonics Rev.*, 2021, **15**, 2100060.

21 L. Jiang, X. Jiang, J. Xie, T. Zheng, G. Lv and Y. Su, Structural induced tunable NIR luminescence of $(Y, Lu)_3(Mg,Al)_2(Al,Si)_3O_{12}$: Cr^{3+} phosphors, *J. Lumin.*, 2022, **247**, 118911.

22 D. Huang, H. Zhu, Z. Deng, H. Yang, J. Hu, S. Liang, D. Chen, E. Ma and W. Guo, A highly efficient and thermally stable broadband Cr^{3+}-activated double borate phosphor for near-infrared light-emitting diodes, *J. Mater. Chem. C*, 2021, **9**, 164–172.

23 Z. Sun, Q. Ning, W. Zhou, J. Luo, P. Chen, L. Zhou, Q. Pang and X. Zhang, Structural and spectroscopic investigation of an efficient and broadband NIR phosphor $InBO_3$: Cr^{3+} and its application in NIR pc-LEDs, *Ceram. Int.*, 2021, **47**, 13598–13603.

24 L. Jiang, X. Jiang, C. Wang, P. Liu, Y. Zhang, G. Lv, T. Lookman and Y. Su, Rapid Discovery of Efficient Long-Wavelength Emission Garnet:Cr NIR Phosphors via Multi-Objective Optimization, *ACS Appl. Mater. Interfaces*, 2022, **14**, 52124–52133.

25 Q. Zhang, D. Liu, P. Dang, H. Lian, G. Li and J. Lin, Two Selective Sites Control of Cr^{3+}-Doped ABO_4 Phosphors for Tuning Ultra-Broadband Near-Infrared Photoluminescence and Multi-Applications, *Laser Photonics Rev.*, 2022, **16**, 2100459.

26 J. Zhong, L. Zeng, W. Zhao and J. Brgoch, Producing Tunable Broadband Near-Infrared Emission through Co-Substitution in $(Ga_{1-x}Mg_x)(Ga_{1-x}Ge_x)O_3:Cr^{3+}$, *ACS Appl. Mater. Interfaces*, 2022, **14**, 51157–51164.

27 C. Zhong, L. Zhang, Y. Xu, X. Wu, S. Yin, X. Zhang and H. You, Novel broadband near-infrared emitting phosphor $LiGe_2(PO_4)_3:Cr^{3+}$ with tuning and enhancement of NIR emission by codoping Sb^{5+}, *J. Alloys Compd.*, 2022, **903**, 163945.

28 T. Yu, H. Sheng, S. Chen, J. Yuan, T. Deng, M. Wu, Y. Guo and Q. Zeng, A broadband near-infrared $Sc_{1-x}(PO_3)_3:XCr^{3+}$ phosphor with enhanced thermal stability and quantum yield by Yb^{3+} codoping, *J. Am. Ceram. Soc.*, 2022, **105**, 3403–3417.

29 F. Zhao, H. Cai, Z. Song and Q. Liu, Structural Confinement toward Controlling Energy Transfer Path for Enhancing Near-Infrared Luminescence, *Chem. Mater.*, 2021, **33**, 8360–8366.

30 C.-H. Lu, Y.-T. Tsai, T.-L. Tsai, T.-S. Chan, X. Zhang and C. C. Lin, Cr^{3+}-Sphere Effect on the Whitlockite-Type NIR Phosphor $Sr_9Sc(PO_4)_7$ with High Heat Dissipation for Digital Medical Applications, *Inorg. Chem.*, 2022, **61**, 2530–2537.

31 F. Y. Zhao, H. Cai, S. Y. Zhang, Z. Song and Q. L. Liu, Octahedron-dependent near-infrared luminescence in Cr^{3+}-activated phosphors, *Mater. Today Chem.*, 2022, **23**, 100704.

32 C. Yuan, R. Li, Y. Liu, L. Zhang, J. Zhang, G. Leniec, P. Sun, Z. Liu, Z. Luo, R. Dong and J. Jiang, Efficient and Broadband $LiGaP_2O_7:Cr^{3+}$ Phosphors for Smart Near-Infrared Light-Emitting Diodes, *Laser Photonics Rev.*, 2021, **15**, 2100227.

33 H. Zhang, J. Zhong, F. Du, L. Chen, X. Zhang, Z. Mu and W. Zhao, Efficient and Thermally Stable Broad-Band Near-Infrared Emission in a $KAlP_2O_7:Cr^{3+}$ Phosphor for Nondestructive Examination, *ACS Appl. Mater. Interfaces*, 2022, **14**(9), 11663–11671.

34 J. Zhong, C. Li, W. Zhao, S. You and J. Brgoch, Accessing High-Power Near-Infrared Spectroscopy Using Cr^{3+}-Substituted Metal Phosphate Phosphors, *Chem. Mater.*, 2022, **34**, 337–344.

35 H. Zhang, J. Zhong, C. Li, L. Wang and W. Zhao, Broadband near-infrared luminescence in the $NaAlP_2O_7$: Cr^{3+} phosphor for spectroscopy applications, *J. Lumin.*, 2022, **251**, 119211.

36 F. Zhao, H. Cai, Z. Song and Q. Liu, Structural Confinement for Cr^{3+} Activators toward Efficient Near-Infrared Phosphors with Suppressed Concentration Quenching, *Chem. Mater.*, 2021, **33**, 3621–3630.

37 S. Miao, Y. Liang, Y. Zhang, D. Chen, S. Yan, J. Liu and X.-J. Wang, Spectrally tunable and thermally stable near-infrared luminescence in $Na_3Sc_2(PO_4)_3:Cr^{3+}$ phosphors by Ga^{3+} co-doping for light-emitting diodes, *J. Mater. Chem. C*, 2022, **10**, 994–1002.

38 B. Bai, P. Dang, D. Huang, H. Lian and J. Lin, Broadband Near-Infrared Emitting $Ca_2LuScGa_2Ge_2O_{12}:Cr^{3+}$ Phosphors: Luminescence Properties and Application in Light-Emitting Diodes, *Inorg. Chem.*, 2020, **59**, 13481–13488.

39 G. Liu, M. S. Molokeev, B. Lei and Z. Xia, Two-site Cr^{3+} occupation in the $MgTa_2O^6:Cr^{3+}$ phosphor toward broadband near-infrared emission for vessel visualization, *J. Mater. Chem. C*, 2020, **8**, 9322–9328.

40 B. Struve and G. Huber, The effect of the crystal field strength on the optical spectra of Cr^{3+} in gallium garnet laser crystals, *Appl. Phys. B*, 1985, **36**, 195–201.

41 D. Huang, X. He, J. Zhang, J. Hu, S. Liang, D. Chen, K. Xu and H. Zhu, Efficient and thermally stable broadband near-infrared emission from near zero thermal expansion

$AlP_3O_9:Cr^{3+}$ phosphors, *Inorg. Chem. Front.*, 2022, **9**, 1692–1700.

42 L. Zeng, J. Zhong, W. Lin and W. Zhao, Achieving a tunable and ultra-broadband near-infrared emission in the $Ga_{2-2x}Zn_xGe_xO_3:Cr^{3+}$ phosphor, *Dalton Trans.*, 2022, **51**, 16740–16747.

43 S. Yu, Z. Wei, J. Wu, T. Wang, J. Zhang, X. Luo, Y. Li, C. Wang and L. Zhao, Design and tuning Cr^{3+}-doped near-infrared phosphors for multifunctional applications via crystal field engineering, *Dalton Trans.*, 2022, **51**, 2313–2322.

44 W. Nie, L. Yao, G. Chen, S. Wu, Z. Liao, L. Han and X. Ye, A novel Cr^{3+}-doped $Lu_2CaMg_2Si_3O_{12}$ garnet phosphor with broadband emission for near-infrared applications, *Dalton Trans.*, 2021, **50**, 8446–8456.

45 D. Hou, H. Lin, Y. Zhang, J.-Y. Li, H. Li, J. Dong, Z. Lin and R. Huang, A broadband near-infrared phosphor $BaZrGe_3O_9:Cr^{3+}$: luminescence and application for light-emitting diodes, *Inorg. Chem. Front.*, 2021, **8**, 2333–2340.

46 Y. Yan, M. Shang, S. Huang, Y. Wang, Y. Sun, P. Dang and J. Lin, Photoluminescence Properties of $AScSi_2O_6:Cr^{3+}$ (A = Na and Li) Phosphors with High Efficiency and Thermal Stability for Near-Infrared Phosphor-Converted Light-Emitting Diode Light Sources, *ACS Appl. Mater. Interfaces*, 2022, **14**, 8179–8190.

47 L. Jiang, X. Jiang, Y. Zhang, C. Wang, P. Liu, G. Lv and Y. Su, Multiobjective Machine Learning-Assisted Discovery of a Novel Cyan–Green Garnet: Ce Phosphors with Excellent Thermal Stability, *ACS Appl. Mater. Interfaces*, 2022, **14**, 15426–15436.

48 L. Jiang, X. Zhang, H. Tang, S. Zhu, Q. Li, W. Zhang, X. Mi, L. Lu and X. Liu, A Mg^{2+}-Ge^{4+} substituting strategy for optimizing color rendering index and luminescence of YAG: Ce^{3+} phosphors for white LEDs, *Mater. Res. Bull.*, 2018, **98**, 180–186.